ORIGINAL PAPER

Numerical Modeling of 3D Hydraulic Fractures Interaction in Complex Naturally Fractured Formations

Olga Kresse[1] · Xiaowei Weng[1]

Abstract

The unconventional fracture model can simulate complex fracture network propagation in a formation with pre-existing natural fractures. The interaction between hydraulic fracture branches, or stress shadowing effect, could be modeled by 2D or 3D displacement discontinuity method (DDM). In this paper, we concentrate on a hydraulic fracture model that integrates 3D DDM for computing the induced 3D stress field around the propagating hydraulic fractures and incorporates the changes in induced stress into the fracture height calculations and propagation criterion. Examples show that for parallel fractures, the height growth may be promoted or suppressed depending on the relative fracture height. For fractures initiated from different formation layers, the fracture growth into the layer occupied by the other fractures is reduced due to the vertical stress shadowing effect.

1 Introduction

Interaction among multiple propagating hydraulic fractures or the so-called stress shadowing effect, especially its influence on fracture propagation path, has been previously studied for fractures initiated and growing in approximately the same formation layers (Kresse et al. 2012). The stress shadowing effect can influence the height growth for fractures propagating in the same layer or in the different layers in depth. The interactions between fractures propagating in height in different vertical layers have not been investigated yet and can have major implications on the success of a fracture treatment.

In this paper, we present a hydraulic fracture model that integrates the constant 3D displacement discontinuity method (3D DDM) for computing the induced 3D stress field around the propagating hydraulic fractures and incorporates the induced stress into the fracture height calculations and propagation criterion.

The displacement discontinuity method is currently widely used to model fracture propagation and interaction. Starting from the work of Crouch and Starfield (1983), this approach has been evolved from two-dimensional constant DDM, to 2D quadratic and higher order DDM, accounting for the different element shapes. The 3D DDM approaches with constant, quadratic, and higher order discontinuities have also been investigated and attract great interest lately (Shou 1993; Shou et al. 1997; Wu 2014). Due to the excessive numerical computation cost associated with the implementation of the full 3D DDM approaches, several simplifications have been made. These simplifications include using 2D DDM with 3D correction factor to account for fracture height effect (Olson 2004), using a simplified form of 3D DDM by neglecting the vertical displacement component, and using 3D height correction factor based on vertically uniform displacement discontinuity (Wu and Olson 2015). The correction factors are derived from the analytical plane strain solution for a uniformly loaded vertical fracture of a finite height (Sneddon 1946), so they are applicable mostly for the cases when the fractures are well contained in the same formation interval.

In this paper, we also adopt a simplified form of the full 3D DDM model for vertical fractures, but consider the fracture height not being restricted in any way. It allows us to

✉ Olga Kresse
  okresse@slb.com

1   Schlumberger, Sugar Land, TX, USA

model the interaction between the fractures initiating and propagating at different depths and in different formation layers. It better accounts for the vertical variation of the induced stress field and gives more accurate prediction of the fracture width and fracture propagation in the hydraulic fracture models based on the Pseudo 3D (P3D) framework.

The simplifications of the 3D DDM for the case of the vertical fractures are implemented without sacrifice of accuracy. The discretization in both vertical and horizontal direction is implemented in the model. The approach is validated against analytical solutions for simple geometries/loading conditions, numerical model, as well as against the enhanced 2D DDM approach previously presented and validated in Kresse et al. (2012).

Examples show that for parallel fractures, the height growth may be promoted or suppressed depending on the relative fracture height. For fractures initiated from different formation layers, a fracture may hinder the other fracture from growing into the layer it occupies due to the vertical stress shadowing effect.

The 3D stress shadow effect is especially important for the multistage fracturing in vertical or deviated wells and multi-well treatments. Examples will demonstrate that 3D stress shadow implementation provides more accurate account of the effect of fractures interaction on fracture width profile and height. It also allows to simulate more accurately the influence between stages in vertical and deviated well, as well as to simulate interference between fracturing stages in stacked horizontal wells targeting different reservoir layers in close proximity.

2 UFM Model Overview

To simulate the propagation of a complex fracture network that consists of many intersecting fractures, the equations governing the underlying physics of the fracturing process must be satisfied. The basic governing equations include equation governing the fluid flow in the fracture network, the equation governing the fracture deformation, and the fracture propagation/interaction criterion.

Continuity equation assumes that fluid flow propagates along fracture network with the following mass conservation:

$$\frac{\partial q}{\partial s} + \frac{\partial (H_{fl} \bar{w})}{\partial t} + q_L = 0, \quad q_L = 2h_L u_L,$$

(1)

where q is the local flow rate inside the hydraulic fracture along the length, $\bar{w}$ is an average width or opening of the fracture at position $s = s(x,y)$, $H_{fl}(s,t)$ is the local height of the fracture occupied by fluid, and q_L is the leak-off volume rate through the wall of the hydraulic fracture into the rock matrix per unit length (leak-off height h_L times velocity u_L at which fracturing fluid infiltrates into surrounding permeable medium), which is expressed through Carter's leak-off model (Carter 1957). The fracture tips propagate as sharp front and the total length of the entire hydraulic fracture networks at any given time t is defined as $L(t)$.

The properties of injected fluid are defined by power-law exponent n' (fluid behavior index) and consistency index K'. The fluid flow could be laminar, turbulent, or Darcy flow through proppant pack, and is described correspondingly by different laws. For the general case of 1D laminar flow of a power-law fluid in any given fracture branch, the Poiseuille law (Mack and Warpinski 2000) can be applied

$$\frac{\partial p}{\partial s} = -\alpha_0 \frac{1}{\bar{w}^{2n'+1}} \frac{q}{H_{fl}} \left| \frac{q}{H_{fl}} \right|^{n'-1}$$

(2)

with

$$\alpha_0 = \frac{2K'}{\phi(n')^{n'}} \cdot \left(\frac{4n'+2}{n'} \right)^{n'}; \quad \phi(n') = \frac{1}{H_{fl}} \int_{H_{fl}} \left(\frac{w(z)}{\bar{w}} \right)^{\frac{2n'+1}{n'}} dz.$$

(3)

Here, $w(z)$ represents fracture width as a function of depth at the current position $s(x, y)$.

Fracture width is related to fluid pressure through the elasticity equation. The elastic properties of the rock (considered as isotropic linear elastic material) are defined by Young's modulus E and Poisson's ratio ν. For a vertical fracture in a layered medium with variable minimum and maximum horizontal stresses [$\sigma_h(x,y,z)$ and $\sigma_H(x,y,z)$] and fluid pressure p, the width profile can be determined from an analytical solution given as

$$w(x, y, z) = w(p(x, y), h, z).$$

(4)

Because the height of the fractures h varies, the set of governing equations also include the height growth calculation based on the approach described in (Kresse et al. 2012)

$$K_{Iu} = \sqrt{\frac{\pi h}{2}} \left[p_{cp} - \sigma_n + \rho_f g \left(h_{cp} - \frac{3}{4} h \right) \right] + \sqrt{\frac{2}{\pi h}} \sum_{i=1}^{n-1} (\sigma_{i+1} - \sigma_i) \left[\frac{h}{2} \arccos \left(\frac{h - 2h_i}{h} \right) - \sqrt{h_i(h - h_i)} \right]$$

$$K_{Il} = \sqrt{\frac{\pi h}{2}} \left[p_{cp} - \sigma_n + \rho_f g \left(h_{cp} - \frac{h}{4} \right) \right] + \sqrt{\frac{2}{\pi h}} \sum_{i=1}^{n-1} (\sigma_{i+1} - \sigma_i) \left[\frac{h}{2} \arccos \left(\frac{h - 2h_i}{h} \right) + \sqrt{h_i(h - h_i)} \right],$$

(5)

where σ_i and h_i are the minimum stress and distance from top of the ith layer to fracture bottom tip, p_{cp} is the fluid pressure at a reference (perforation) depth h_{cp} measured from the bottom tip, and K_{Iu} and K_{Il} are the stress intensity factors at the top and bottom tips of the fracture.

The equilibrium model, which calculates fracture height based on the pressure at each position of the fracture by matching stress intensity factors K_{Iu} and K_{Il}, given by Eq. (5), to the fracture toughness of the corresponding layer containing the tips, is extended to a non-equilibrium model (Mack and Warpinski 2000). The non-equilibrium height growth calculation takes into account the pressure gradient due to the fluid flow in the tip regions in the vertical direction by adding apparent toughness proportional to the fracture's top and bottom velocities. Then, fracture width $w(z)$ at any position z measured from the bottom tip is given by Eq. (6), where E' is the averaged plane strain modulus

$$
w(z) = \frac{4}{E'} \left[p_{cp} - \sigma_n + \rho_f g \left(h_{cp} - \frac{h}{4} - \frac{z}{2} \right) \right] \sqrt{z(h-z)}
$$
$$
+ \frac{4}{\pi E'} \sum_{i=1}^{n-1} (\sigma_{i+1} - \sigma_i) \left[\begin{array}{l} (h_i - z)\cosh^{-1} \dfrac{z\left(\frac{h-2h_i}{h} \right) + h_i}{|z - h_i|} \\ + \sqrt{z(h-z)} \arccos \left(\dfrac{h - 2h_i}{h} \right) \end{array} \right].
$$

(6)

Note that one of the limitations of UFM model, the same as for the conventional P3D models, is related to the accurate height growth calculations in the cases of complicated vertical stress profile. For the height being calculated for each fracture element, UFM model assumes that reservoir elastic properties are homogeneous, and averaged over all layers containing fracture height. Since confining stress dominates elastic properties when computing fracture width, this assumption is reasonable for many cases (Adachi et al. 2007). P3D models' results are in good agreement with Planar3D models for not too complex stress profiles, and present fast and accurate engineering tools for most field applications. To overcome some limitations of the P3D model, the Stacked Height Model option was developed (Cohen et al. 2015).

In addition to equations described above, the global volume balance condition must be satisfied

$$
\int_0^t Q(t)dt = \int_0^{L(t)} h(s,t)\bar{w}(s,t)ds + \int_{H_L} \int_0^t \int_0^{L(t)} 2u_L \, ds \, dt \, dh_L \quad (7)
$$

i.e., the total volume of fluid pumped during time t is equal to volume of fluid in fracture network and volume leaked from the fracture up to time t. The boundary conditions require the flow rate, net pressure, and fracture width to be zero at all fracture tips. The total network consists of two major parts: Fracture Network and Wellbore. These two networks communicate through injection elements to account for perforation friction.

The system of Eqs. (1–7), together with initial and boundary conditions, plus equations governing fluid flow in the wellbore and through the perforations represent the complete set of governing equations (Kresse et al. 2012). Combining these equations and discretizing the fracture network into small elements leads to a nonlinear system of equations in terms of fluid pressure p in each element, simplified as $f(p) = 0$, which is solved using damped Newton–Raphson method.

Fracture interaction is one of the most important factors which must be taken into account to model hydraulic fracture propagation in naturally fractured reservoirs. This includes the interaction between hydraulic fractures and natural fractures, as well as interaction between hydraulic fractures. For the interaction between hydraulic and natural fractures, an OpenT crossing model, accounting for the fluid properties in addition to the rock and natural fractures properties, was implemented (Kresse et al. 2013).

This paper focuses on modeling the interaction between hydraulic fractures, especially on the importance to account for the 3D effect.

Notice, that poroelastic effects currently are not included in UFM model. It is observed that in unconventional formation (shales) changes in pore pressure due to leak-off into the matrix are of inches from the fracture so poroelastic effect may be considered negligible (Detournay and Cheng 1993).

3 Modeling Stress Shadow

3.1 2D DDM Approach

For complex fracture networks, when fractures may orient in different directions and intersect each other, to compute the effective stress on any given fracture branch from the rest of the fracture network, an enhanced 2D Displacement Discontinuity Method (DDM) (Fig. 1) was originally implemented in UFM (Kresse et al. 2012).

In a 2D, plane strain, displacement discontinuity solution, Crouch and Starfield (1983) described the normal and shear stresses (σ_n and σ_s) acting on one fracture element induced by the opening and shearing displacement discontinuities (D_n and D_s) from all fracture elements. To account for the 3D effect due to finite fracture height, Olson (2004) introduced a 3D correction factor to the influence coefficients C^{ij}. The modified elasticity equations of 2D DDM are as follows:
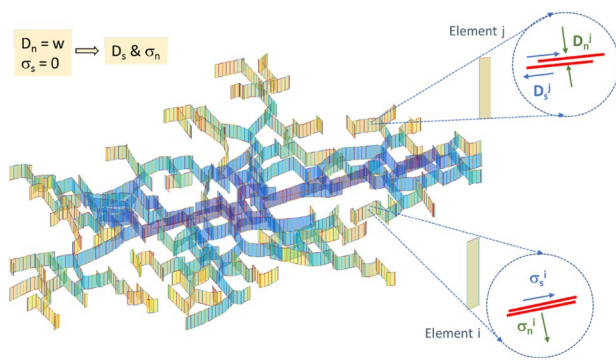
Fig. 1 Schematics of the 2D stress shadow effect

$$\sigma_n^i = \sum_{j=1}^{N} A^{ij} C_{ns}^{ij} D_s^j + \sum_{j=1}^{N} A^{ij} C_{nn}^{ij} D_n^j$$

$$\sigma_s^i = \sum_{j=1}^{N} A^{ij} C_{ss}^{ij} D_s^j + \sum_{j=1}^{N} A^{ij} C_{sn}^{ij} D_n^j, \tag{8}$$

where C^{ij} are the 2D, plane strain elastic influence coefficients, and their expressions can be found in Crouch and Starfield (1983). The matrix $[C]$ defines the interaction between elements, for example $C_{ns}{}^{ij}$ gives the normal stress at the midpoint of the element i due to shear displacement discontinuity at the element j, and $C_{nn}{}^{ij}$ gives the normal stress at the midpoint of the element i due to an opening displacement discontinuity at the element j. The 3D correction factor A^{ij} suggested by Olson (2004) was introduced to the influence coefficients to account for the 3D effects due to finite fracture height that leads to decaying of interaction between any two fracture elements when distance between them increases

$$A^{ij} = 1 - \frac{d_{ij}^{\beta}}{\left[d_{ij}^2 + (h/\alpha)^2\right]^{\beta/2}}, \tag{9}$$

where h is the fracture height, d_{ij} is the distance between elements i and j, $\alpha = 1$ and $\beta = 3.2$ are empirically derived constants (Olson 2008; Laubach et al. 2004). Equation (9) clearly shows that the 3D correction factor leads to decaying of interaction between any two fracture elements when the distance increases.

In UFM model, at each time step, the additional induced stresses due to the stress shadow effects are computed. We assume that at any time, fracture width equals the normal displacement discontinuities (D_n) and shear stress at the fracture surface is zero, i.e., $D_n^j = w_j$, $\sigma_s^i = 0$. Substituting these two conditions into Eq. (8), we can find the shear displacement discontinuities D_s and normal stress induced on each fracture element σ_n.

The effects of the stress shadow induced stresses on the fracture network propagation pattern are twofold. First, during pressure and width iteration, the original in situ stresses at each fracture element are modified by adding the additional normal stress due to the stress shadow effect. This directly affects the fracture pressure and width distribution which results in a change on the fracture growth. Second, by including the stress shadow induced stresses (normal and shear stresses), the local stress fields ahead the propagating tips are also altered which may cause the local principal stress direction to deviate from the original in situ stress direction.

Thus, the local stresses around each tip element σ_{xx}^{tip}, σ_{yy}^{tip}, σ_{xy}^{tip} calculated by enhanced DDM approach are combined with far-field stresses σ_{xx}^{∞}, σ_{yy}^{∞}, σ_{xy}^{∞}

$$\begin{aligned}
\sigma_{xx}^{\text{tot}} &= \sigma_{xx}^{\infty} + \sigma_{xx}^{\text{tip}} \\
\sigma_{yy}^{\text{tot}} &= \sigma_{yy}^{\infty} + \sigma_{yy}^{\text{tip}} \\
\sigma_{xy}^{\text{tot}} &= \sigma_{xy}^{\infty} + \sigma_{xy}^{\text{tip}}
\end{aligned} \tag{10}$$

to define local principal stresses and orientation (angle α) of local maximum stress around tip elements by

$$\sigma_1 = \frac{\sigma_{xx}^{\text{tot}} + \sigma_{yy}^{\text{tot}}}{2} + \sqrt{(\sigma_{xy}^{\text{tot}})^2 + \frac{(\sigma_{xx}^{\text{tot}} - \sigma_{yy}^{\text{tot}})^2}{4}}$$

$$\sigma_3 = \frac{\sigma_{xx}^{\text{tot}} + \sigma_{yy}^{\text{tot}}}{2} - \sqrt{(\sigma_{xy}^{\text{tot}})^2 + \frac{(\sigma_{xx}^{\text{tot}} - \sigma_{yy}^{\text{tot}})^2}{4}} \tag{11}$$

$$\alpha = \frac{1}{2} \arctan \left| \frac{2\sigma_{xy}^{\text{tot}}}{\sigma_{xx}^{\text{tot}} - \sigma_{yy}^{\text{tot}}} \right|.$$

This altered local principal stress direction may result in fracture turning from its original propagation plane and further affects the fracture network propagation pattern.

Notice that 2D stress shadow implementation, where the average induced stresses on any given element are computed based on the 2D DDM equation, does not consider the vertical variation of the induced stresses. This could be acceptable when different branches have similar height and initiated at the same layer (Fig. 2). At the same time when fracture branches are vertically offset or initiated in different layers and have different heights, the results from 2D stress shadow effect might not be accurate (Fig. 4a).

3.2 3D DDM Approach

The 3D constant displacement discontinuity method is based on the analytical solution to the problem of a constant displacement discontinuity over a finite rectangular element $|x_1| \leq a$, $|x_2| \leq b$, $x_3 = 0$ in an infinite elastic medium.
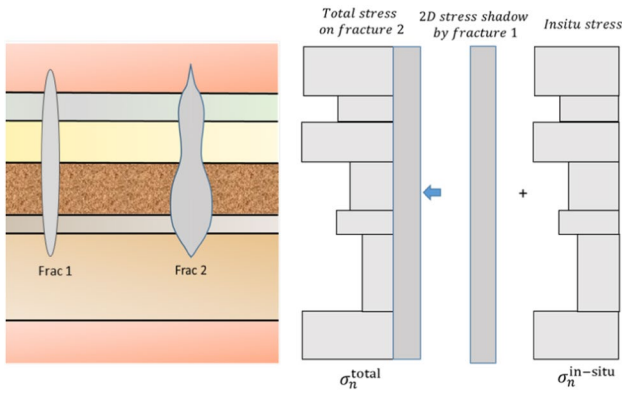
Fig. 2 Illustration of 2D stress shadow effect from fracture 1 on fracture 2. Fractures have similar height and are initiated at the same layer

Consider the 3D fracture as a collection of rectangular elements (Fig. 3), where x_1, x_2, x_3 is the local coordinate system of the displacement discontinuity element, in which x_3 is normal to the element plane. Each element has a positive $(x_3 = 0^+)$ side and a negative $(x_3 = 0^-)$ side.

Crossing from one side of the displacement discontinuity element to the other side, the displacements u_1, u_2, u_3 undergo a jump, given by (Shou 1993)

$$D_1(x_1, x_2, 0) = u_1(x_1, x_2, 0^-) - u_1(x_1, x_2, 0^+)$$
$$D_2(x_1, x_2, 0) = u_2(x_1, x_2, 0^-) - u_2(x_1, x_2, 0^+) \qquad (12)$$
$$D_3(x_1, x_2, 0) = u_3(x_1, x_2, 0^-) - u_3(x_1, x_2, 0^+),$$

where D_1 and D_2 are the shear displacement discontinuities and D_3 is the normal displacement discontinuity for element i, $D_i = (D_1, D_2, D_3)$. A negative value of D_3 corresponds to a positive opening width.

The analytical expressions for the stress components σ_{ij}, $i, j, = 1, 2, 3$ induced by constant shear and normal displacement discontinuities given in Eq. (12) over a rectangular element $|x_1| \le a$, $|x_2| \le b$, $x_3 = 0$ in an infinite elastic medium in the local coordinate system, at any observation point x_1, x_2, x_3, have the form
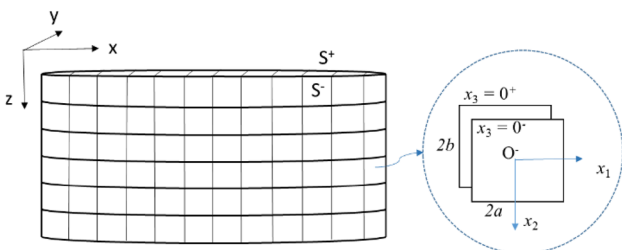
Fig. 3 A three-dimensional crack in an infinite elastic solid media (similar to Wu and Olson 2015, different axes orientation)

$$\sigma_{11} = C_r\big[(2I_{,13} - x_3 I_{,111})D_1 + (2\nu I_{,23} - x_3 I_{,211})D_2$$
$$+ (I_{,33} + (1 - 2\nu)I_{,22} - x_3 I_{,311})D_3\big]$$
$$\sigma_{22} = C_r\big[(2\nu I_{,13} - x_3 I_{,122})D_1 + (2I_{,23} - x_3 I_{,222})D_2$$
$$+ (I_{,33} + (1 - 2\nu)I_{,11} - x_3 I_{,322})D_3\big]$$
$$\sigma_{33} = C_r\big[-x_3 I_{,133}D_1 - x_3 I_{,233}D_2 + (I_{,33} - x_3 I_{,333})D_3\big]$$
$$\sigma_{12} = C_r\big[((1 - \nu)I_{,23} - x_3 I_{,112})D_1 + ((1 - \nu)I_{,13} - x_3 I_{,212})D_2$$
$$- ((1 - 2\nu)I_{,12} + x_3 I_{,312})D_3\big]$$
$$\sigma_{13} = C_r\big[(I_{,33} + \nu I_{,22} - x_3 I_{,113})D_1 - (\nu I_{,12} + x_3 I_{,213})D_2$$
$$- x_3 I_{,313}D_3\big]$$
$$\sigma_{23} = C_r\big[(-\nu I_{,21} - x_3 I_{,123})D_1 + (I_{,33} + \nu I_{,11} - x_3 I_{,223})D_2$$
$$- x_3 I_{,323}D_3\big]. \qquad (13)$$

This solution has been first derived by Rongved (1957) and Salamon (1964), and lately revisited by Wu (2014). Here, ν is the Poisson's ratio, G is the shear modulus, and

$$C_r = \frac{G}{4\pi(1 - \nu)}$$

$$I(x_1, x_2, x_3) = \int_{-b}^{b} \int_{-a}^{a} \frac{d\xi_1 d\xi_2}{\sqrt{(x_1 - \xi_1)^2 + (x_2 - \xi_2)^2 + x_3^2}}. \qquad (14)$$

Also $I_{,k}$, $I_{,kl}$, $I_{,klm}$ are first-, second-, and third-order derivatives of I with respect to coordinate x_k, x_l, x_m, respectively. The detailed derivation of Eq. (13) together with expressions for the derivatives of the kernel analytical function I in Eq. (13) could be found in Shou (1993), Wu (2014) and will not be repeated here.

The corresponding expressions for the displacements are

$$u_1 = \frac{C_r}{2G}\big\{D_1[2(1 - \nu)I_3 - x_3 I_{,11}] + D_2[-x_3 I_{,21}]$$
$$+ D_3[-(1 - 2\nu)I_{,1} - x_3 I_{,31}]\big\}$$
$$u_2 = \frac{C_r}{2G}\big\{D_1[-x_3 I_{,12}] + D_2[2(1 - \nu)I_3 - x_3 I_{,22}]$$
$$+ D_3[-(1 - 2\nu)I_{,2} - x_3 I_{,32}]\big\}$$
$$u_3 = \frac{C_r}{2G}\big\{D_1[(1 - 2\nu)I_{,1} - x_3 I_{,13}] + D_2[(1 - 2\nu)I_{,2} - x_3 I_{,23}]$$
$$+ D_3[2(1 - \nu)I_3 - x_3 I_{,33}]\big\}. \qquad (15)$$

For the numerical implementation, the fracture surfaces are discretized into a grid of N rectangular elements, with each element having constant displacement discontinuities (D_1, D_2, D_3). Each rectangular element has its own local coordinate system. The displacement and stress fields at the midpoint of the ith element due to constant displacement discontinuities D_1^j, D_2^j, D_3^j over the jth element have the forms given in Eqs. (13) and (15) in the local coordinate system, which can be transformed to be expressed in the global

coordinate system. Subsequently, the displacement and stress components at the midpoint of the ith element due to constant shear and normal displacement discontinuities over all N elements can be obtained by summing the contribution of each individual elements in the network, i.e., they have the form

$$u_1^i = \sum_{j=1}^{N} [B_{11}^{ij}D_1^j + B_{12}^{ij}D_2^j + B_{13}^{ij}D_3^j]$$

$$u_2^i = \sum_{j=1}^{N} [B_{21}^{ij}D_1^j + B_{22}^{ij}D_2^j + B_{23}^{ij}D_3^j] \qquad (16)$$

$$u_3^i = \sum_{j=1}^{N} [B_{31}^{ij}D_1^j + B_{32}^{ij}D_2^j + B_{33}^{ij}D_3^j],$$

and

$$\sigma_{11}^i = \sum_{j=1}^{N} [A_{111}^{ij}D_1^j + A_{112}^{ij}D_2^j + A_{113}^{ij}D_3^j]$$

$$\sigma_{22}^i = \sum_{j=1}^{N} [A_{221}^{ij}D_1^j + A_{222}^{ij}D_2^j + A_{223}^{ij}D_3^j]$$

$$\sigma_{33}^i = \sum_{j=1}^{N} [A_{331}^{ij}D_1^j + A_{332}^{ij}D_2^j + A_{333}^{ij}D_3^j]$$

$$\qquad (17)$$

$$\sigma_{12}^i = \sum_{j=1}^{N} [A_{121}^{ij}D_1^j + A_{122}^{ij}D_2^j + A_{123}^{ij}D_3^j]$$

$$\sigma_{13}^i = \sum_{j=1}^{N} [A_{131}^{ij}D_1^j + A_{132}^{ij}D_2^j + A_{133}^{ij}D_3^j]$$

$$\sigma_{23}^i = \sum_{j=1}^{N} [A_{231}^{ij}D_1^j + A_{232}^{ij}D_2^j + A_{233}^{ij}D_3^j]$$

here $A_{knl}^{ij}, B_{kn}^{ij}$, k, n, $l = 1$, 2, 3 are the boundary influence coefficients for stresses and displacements correspondingly. For the case of vertical fractures (Fig. 3), the shear and normal stress components at the midpoint of the i th element due to constant shear and normal displacement discontinuities D_1^j, D_2^j, D_3^j over the j th element in the local coordinate system of ith element will have the form

$$\sigma_{s1}^i = \sigma_{13}'^i = \left[A_{131}^{ij}D_1^j + A_{132}^{ij}D_2^j + A_{133}^{ij}D_3^j \right]$$

$$\sigma_{s2}^i = \sigma_{23}'^i = \left[A_{231}^{ij}D_1^j + A_{232}^{ij}D_2^j + A_{233}^{ij}D_3^j \right] \qquad (18)$$

$$\sigma_n^i = \sigma_{33}'^i = \left[A_{331}^{ij}D_1^j + A_{332}^{ij}D_2^j + A_{333}^{ij}D_3^j \right],$$

where the local coordinates (x_1, x_2, x_3) of the midpoint of the i -th element (x^i, y^i, z^i) relate to the local coordinate system of the j th element via coordinate transformation

$$x_1 = \cos\beta^j (x^i - x^j) + \sin\beta^j (y^i - y^j)$$

$$x_2 = (z^i - z^j) \qquad (19)$$

$$x_3 = -\sin\beta^j (x^i - x^j) + \cos\beta^j (y^i - y^j),$$

where (x^j, y^j, z^j) is the global coordinate of the midpoint of the jth element. Here β^j is the angle between x_1-axis (local coordinate system of element j) and x-axis (global coordinate system).

The influence coefficients in Eq. (18) have the form (where $\gamma = \beta^i - \beta^j$)

$$A_{131}^{ij} = \frac{G}{4\pi(1-v)}\left[v\cos 2\gamma I_{,22} + \cos 2\gamma I_{,33} - \sin 2\gamma I_{,13} - x_3(-\cos\gamma\sin\gamma I_{,111} + \sin\gamma\cos\gamma I_{,133} + \cos 2\gamma I_{,113}) \right]$$

$$A_{132}^{ij} = \frac{G}{4\pi(1-v)}\left[-v\cos 2\gamma I_{,12} - v\sin 2\gamma I_{,23} - x_3(-\cos\gamma\sin\gamma I_{,211} + \sin\gamma\cos\gamma I_{,233} + \cos 2\gamma I_{,213}) \right]$$

$$A_{133}^{ij} = \frac{G}{4\pi(1-v)}\left[-(1-2v)\cos\gamma\sin\gamma I_{,22} - x_3(-\cos\gamma\sin\gamma I_{,311} + \sin\gamma\cos\gamma I_{,333} + \cos 2\gamma I_{,313}) \right]$$

$$A_{231}^{ij} = \frac{G}{4\pi(1-v)}\left[-v\cos\gamma I_{,21} - (1-v)\sin\gamma I_{,23} - x_3(-\sin\gamma I_{,112} + \cos\gamma I_{,123}) \right]$$

$$A_{232}^{ij} = \frac{G}{4\pi(1-v)}\left[v\cos\gamma I_{,11} + \cos\gamma I_{,33} - (1-v)\sin\gamma I_{,13} - x_3(-\sin\gamma I_{,212} + \cos\gamma I_{,223}) \right]$$

$$A_{233}^{ij} = \frac{G}{4\pi(1-v)}\left[+(1-2v)\sin\gamma I_{,12} - x_3(-\sin\gamma I_{,312} + \cos\gamma I_{,323}) \right]$$

$$A_{331}^{ij} = \frac{G}{4\pi(1-v)}\left[-v\sin 2\gamma I_{,22} - \sin 2\gamma I_{,33} + 2\sin^2\gamma I_{,13} - x_3(\sin^2\gamma I_{,111} + \cos^2\gamma I_{,133} - \sin 2\gamma I_{,113}) \right]$$

$$A_{332}^{ij} = \frac{G}{4\pi(1-v)}\left[+v\sin 2\gamma I_{,12} + 2v\sin^2\gamma I_{,23} - x_3(\sin^2\gamma I_{,211} + \cos^2\gamma I_{,233} - \sin 2\gamma I_{,213}) \right]$$

$$A_{333}^{ij} = \frac{G}{4\pi(1-v)}\left[(1-2v)\sin^2\gamma I_{,22} + I_{,33} - x_3(\sin^2\gamma I_{,311} + \cos^2\gamma I_{,333} - \sin 2\gamma I_{,313}) \right].$$

$$\qquad (20)$$

The shear and normal stresses at the midpoint of the ith element due to constant shear and normal displacement discontinuities over all N elements in the fracture network can be obtained by summing the contribution of each individual element as presented earlier, i.e.,

$$\sigma_{s1}^i = \sum_{j=1}^{N} \left[A_{s1s1}^{ij} D_{s1}^j + A_{s1s2}^{ij} D_{s2}^j + A_{s1n}^{ij} D_{n}^j \right]$$

$$\sigma_{s2}^i = \sum_{j=1}^{N} \left[A_{s2s1}^{ij} D_{s1}^j + A_{s2s2}^{ij} D_{s2}^j + A_{s2n}^{ij} D_{n}^j \right] \qquad (21)$$

$$\sigma_{n}^i = \sum_{j=1}^{N} \left[A_{ns1}^{ij} D_{s1}^j + A_{ns2}^{ij} D_{s2}^j + A_{nn}^{ij} D_{n}^j \right].$$

For the special case of the vertical hydraulic fractures the influence coefficients in Eq. (21) are related to Eq. (20) as

$$A_{s1s1}^{ij} = A_{131}^{ij}, \ A_{s1s2}^{ij} = A_{132}^{ij}, \ A_{s1n}^{ij} = A_{133}^{ij},$$
$$A_{s2s1}^{ij} = A_{231}^{ij}, \ A_{s2s2}^{ij} = A_{232}^{ij}, A_{s2n}^{ij} = A_{233}^{ij}, \qquad (22)$$
$$A_{ns1}^{ij} = A_{331}^{ij}, \ A_{ns2}^{ij} = A_{332}^{ij}, A_{nn}^{ij} = A_{333}^{ij}.$$

We will use the 3D stress shadow given in Eq. (21) to better predict the fracture growth in height. Without ignoring the shearing in the dip-slip mode (as in Wu and Olson 2015), we use two shear components of displacement discontinuity together with one normal component $(D_1, D_2, D_3) = (D_{s1}, D_{s2}, D_n)$ in our calculations.

The fundamental difference between 2D and 3D stress shadow effects on the fracture height growth is illustrated in Fig. 4, where two vertically offset fractures propagating in a formation consisting of multiple layers with piece-wise constant in situ minimum horizontal stress. The 2D stress shadow calculation gives an additional constant induced stress by fracture 1 on top of the in situ stress field at the fracture 2 (x, y) location (Fig. 4a). But if the 3D stress shadow corrections are calculated at the center of each layer at the (x, y) location of fracture element, we will have a vertically variable induced stress shadow, leading to a different and more accurate vertical stress profile (Fig. 4b). The induced normal stress is compressive within approximately the depth interval of the fracture 1, and tensile above and below the fracture 1. The width profile of the elements in fracture 2 as well as fracture growth in height calculated with 3D DDM approach will be more accurate and realistic.

4 Implementation of 3D DDM-Based Stress Shadow Calculations

The 3D DDM approach outlined above has been implemented in a P3D-based complex fracture network model which previously used 2D DDM for computing the stress

shadow (Kresse et al. 2012). Each fracture element can be discretized in an arbitrary number of elements N_{height} along the fracture height direction (see Fig. 5 with $N_{\text{height}} = 31$).

One of the major assumptions and simplification in a P3D model is the vertical fracture width profile can be approximately calculated in each vertical element from the 2D elasticity equation based on the local fluid pressure and stress profile. This reduces the fracture problem from a 3D to a 2D problem and drastically reduces the computation time. For a layered formation with piece-wise constant stress, the width can be expressed in analytical form (Nolte and Economides 2000; Fung et al. 1987) shown in Eq. (6). A similar set of analytical expressions is available for the Mode I stress intensity factors at the top and bottom tips of the fracture that are solved to determine the fracture height and the tip positions (Eq. 5).

A major advantage of a P3D-based model is that it can cope with very complex layered formation with arbitrary layer thicknesses which is a commonplace and would present a big challenge to a numerical grid-based code to have sufficient resolution to capture the detailed layers. However, the P3D Eq. (6) does not account for the mechanical interaction with the adjacent fractures. To retain the computational efficiency of the P3D model, the interaction among the fractures is taken into account through an induced stress (i.e., the stress shadow) that is added to the in situ stress whose influence on fracture width is given in Eq. (6). Therefore, the 3D DDM Eq. (21) is not solved directly for the displacement discontinuities D_{s1}, D_{s2}, and D_n. Instead, normal displacement discontinuity $D_n = -w$ is obtained from P3D Eq. (6) in each element, and used in Eq. (21) to compute D_{s1}, D_{s2} by solving the first two sets of equations in Eq. (21) with zero (far field) shear stresses. The induced normal stress component is computed from the last set of Eq. (21), with the summation carried over the elements of the neighboring fractures.

The main algorithm for the 3D stress shadow calculations implemented in the complex fracture model (UFM) is shown on Fig. 6 and is similar to the 2D DDM stress shadow approach (Kresse et al. 2012).

It is worth mentioning that there are different options for stress shadow calculations which are implemented in the code, such as to use 2D or 3D stress shadow approach, use full or simplified 3D DDM, to account for the contributions from the vertical shear component or not, how many elements in vertical discretization to use (N_{height}), and how many normal displacement discontinuities to use while calculating the shear DD components.

At each time step, the shear DDs and additional normal stress caused by the 3D stress shadow effect are computed for each fracture element at the position of element center (x, y), and at the midpoint of each vertical layer (zone) by summing the contribution of all DD elements. The $N_{\text{height}} - 2$

Fig. 4 Illustration of 2D (**a**) and 3D (**b**) stress shadow effect from fracture 1 on fracture 2 when fractures are initiated at different depths
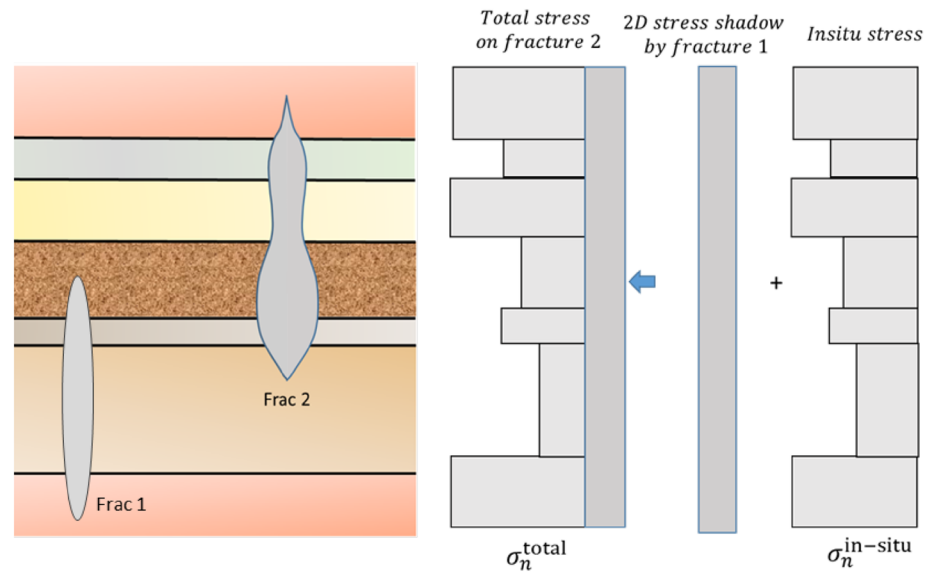
(**a**) Illustration of 2D stress shadow effect from fracture 1 on fracture 2
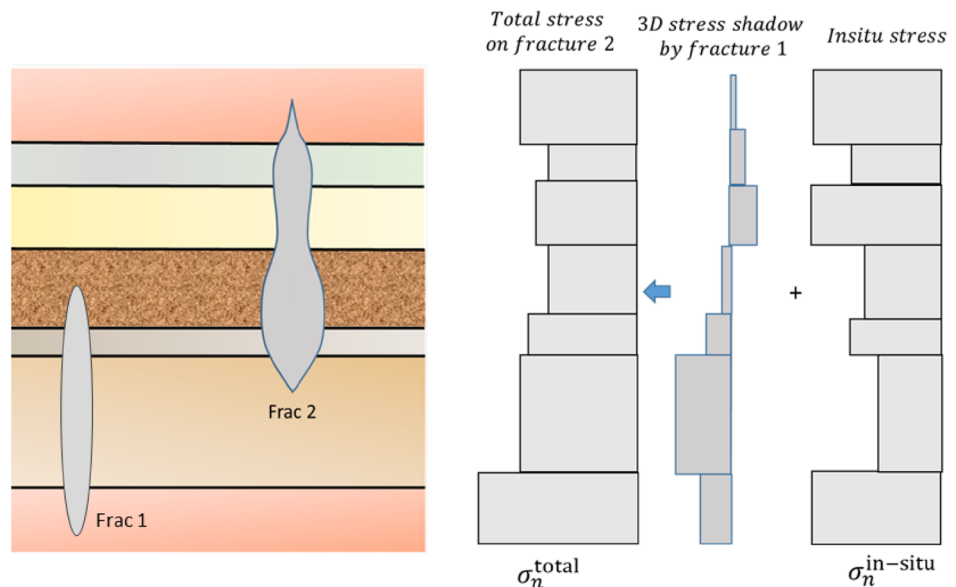
(**b**) 3D stress shadow effect from fracture 1 on fracture 2

DD elements are used for calculating the contribution of both shear and normal DDs to the normal component of the induced stresses. The contribution from the elements which are far away from the zone center is neglected.

To avoid singularity along the border of the source element (see the next section) when it is too close to the receiver element either horizontally or vertically, the normal component of the induced stresses is calculated as the linear interpolation between the stress shadow values computed at the projected points of the centers of the four closest DD elements on the receiver element's plane.

The additional normal stress field caused by the 3D stress shadow effect is then added to the normal component of the in situ stress field acting on each fracture element over each zone (Fig. 3b, on the right). Moreover, the stress shadow induced stresses are computed at a small distance ahead of all fracture tips which is used in determining the direction of incremental fracture tip propagation along with the computed stress intensity factors at the tips.

The stress shadow from the fractures in the previous stages is accounted for in the 3D stress shadow calculation in a similar way as in 2D stress shadow. The calculated
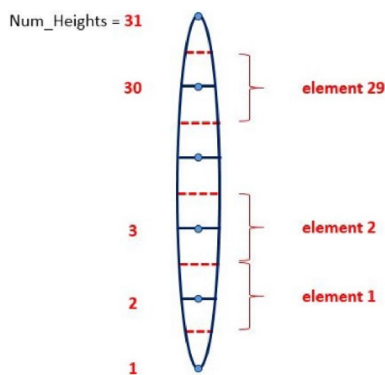
Fig. 5 Discretization of the fracture element with $N_{\text{height}} = 31$
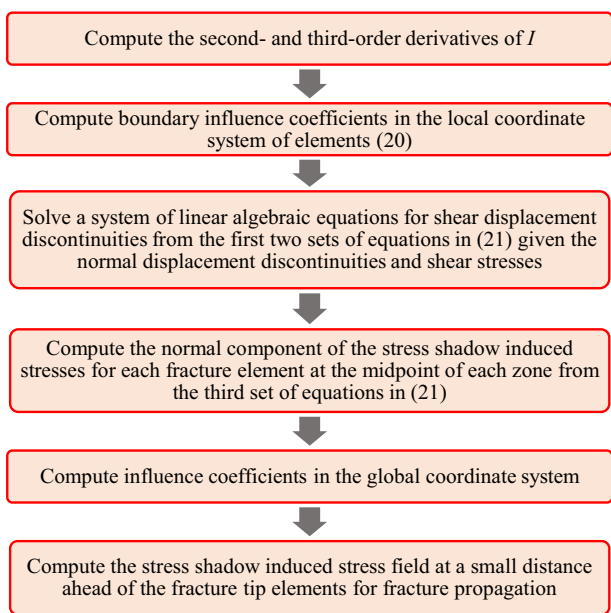
Fig. 6 3D DDM implementation

numerical stress shadow from previous stage is replaced by pre-calculated analytical solution in some situations when distance between elements is small. If elements from the current and previous stages belong to the same fracture plane the projection method is used to avoid possible singularities. Stress shadow calculations are performed at the projected points and then interpolation is performed to obtain the value at the receiver point.

Some of the potential issues related to the implementation of the 3D DDM approach for stress shadow calculations in a complex simulator are the memory issue and the computational efficiency. For example, if each fracture element is discretized into $N_{\text{height}} - 2 = 29$ (with $N_{\text{height}} = 31$) elements along the fracture height direction, assuming that the number of hydraulic fracture elements (not including wellbore elements) is N_{ele}, the total number of displacement discontinuity elements N will be $N = N_{\text{ele}} \times (N_{\text{height}} - 2)$. To obtain the shear components of the displacement discontinuity (D_{s1}^{j} and D_{s2}^{j}), we need to solve a system of linear algebraic equations in which the order of the matrix is $2N$ ($2N \times 2N$ matrix). Considering that double-precision floating-point format occupies eight bytes in computer memory, we will need $2N \times 2N \times 8 \times 10^{-9}$ GB of memory. For a problem with $N_{\text{ele}} = 1000$, which is not uncommon in complex fracture simulations, the stiffness matrix alone occupies approximately 27 GB of memory, severely limiting its applicability and performance.

To alleviate the potential memory issue and reduce the computational cost, one alternative is to reduce the number of discretization along the fracture height direction. Exclusion of the stress shadow from the far-away elements also helps reduce CPU time and memory. Another alternative is to use the simplified 3D DDM method, in which the shear displacement discontinuity along the fracture height direction (D_{s2}^{j}) is ignored. This simplification reduces the order of the matrix from $2N$ to N. Therefore, the unknown shear displacement discontinuity along the fracture length (D_{s1}^{j})

Fig. 7 Anisotropic stress field with distance between the initiation points in the y direction of 10 m. **a** Five vertical DD elements are used. **b** Ten vertical DD elements are used
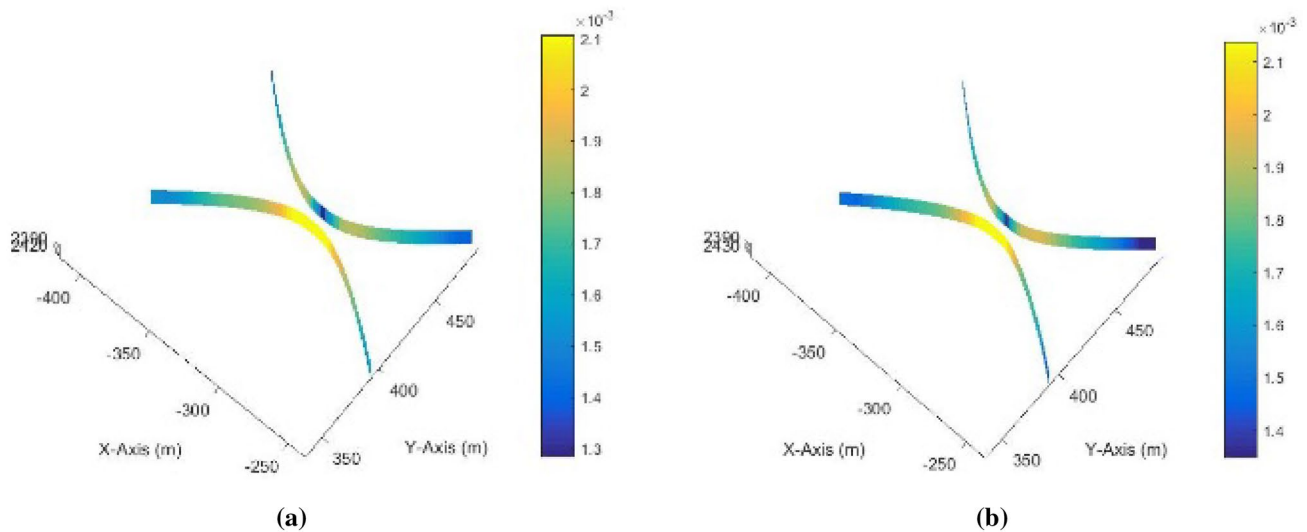

(a)

(b)
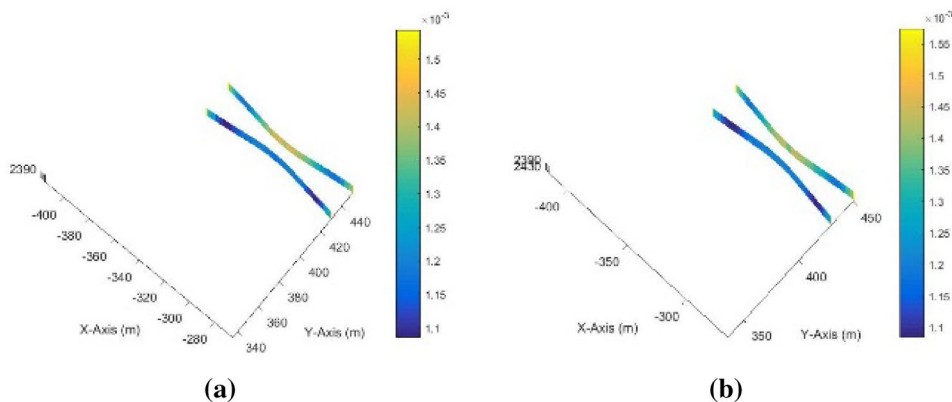
Fig. 8 Isotropic stress field with distance between the initiation points in the y direction of 10 m. **a** Five DD elements are used. **b** Ten DD elements are used
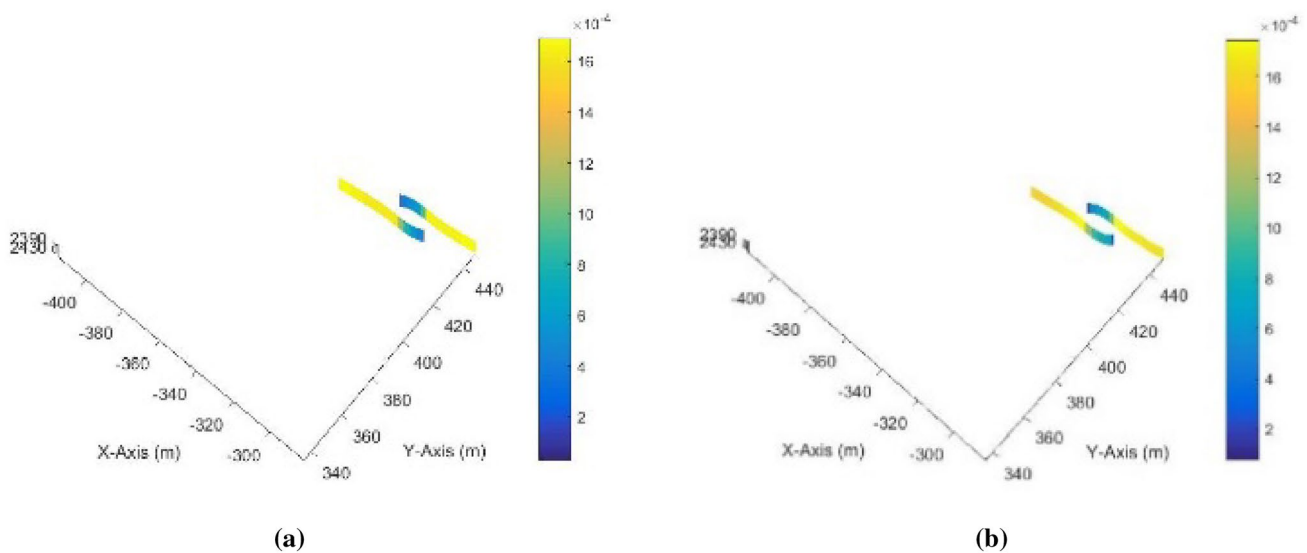

Fig. 9 Isotropic stress field with distance between the initiation point of 10 m in the x and y directions. **a** Five DD elements are used. **b** Ten DD elements are used

can be obtained by solving a system of *N* linear algebraic equations. Both alternatives can result in the loss of fidelity and reduced accuracy.

In this study, we investigated the consequences of reducing the number of vertical discretization elements for calculation of the shear DD components. By considering the vertical discretization with varying number of elements of 31, 12, 10, and 5, we saw that without sacrificing too much accuracy we can use a discretization of each vertical fracture element into 5 DD elements. The comparison of the results simulated with ten and five elements for the constant height

fractures is shown in Figs. 7, 8 and 9 with no visible difference in results (Kresse et al. 2017). The scale corresponds to the fracture width, and fracture width and shape have been compared. The choice of vertical discretization precision of course depends also on the complexity of the problem, including the number of vertical layers and height of the fractures.

At the same time since the stress shadow is calculated at the middle of each zone using the projection method and interpolation, the number of zones could also affect the simulation time. If the zone height is small and the properties of

Fig. 10 Normal and shear displacement discontinuities along the fracture length (31 × 31 mesh) for a fracture under plane strain conditions
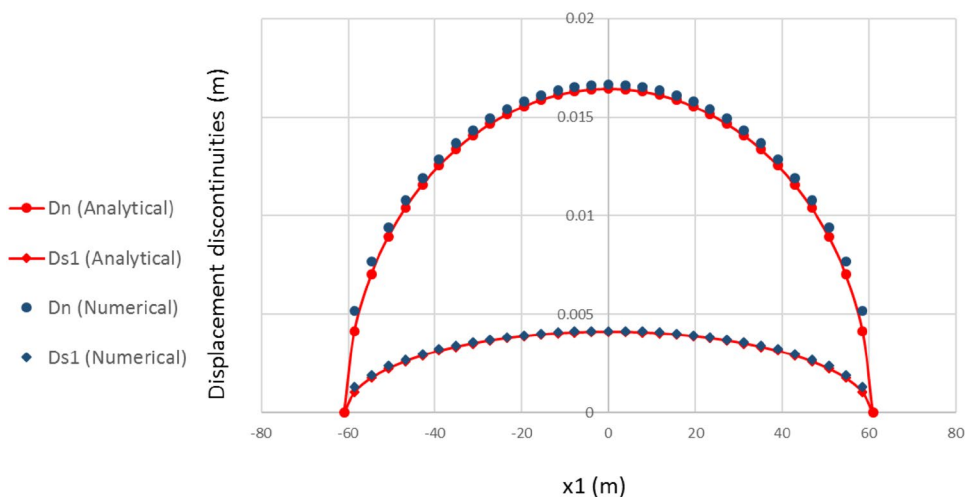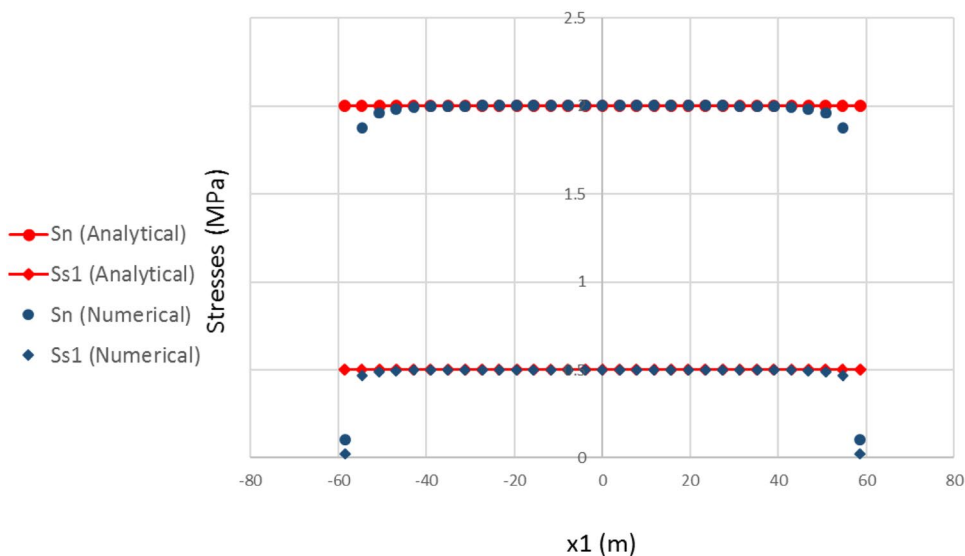

Fig. 11 Comparison of computed stresses for a fracture under plane strain conditions with specified DDs

neighboring zones do not vary too much, some zones could be combined to accelerate the stress shadow calculations without too much of effect on accuracy.

5 Validation of 3D Stress Shadow Implementations

The 3D stress shadow implementation has been validated against analytical and numerical solutions.

5.1 Plane Strain Fracture Subject to Internal Normal and Shear Stresses

To validate 3D stress shadow implementation, a comparison is made with the analytical solution for a plane strain fracture under uniform internal normal and shear stress given in Pollard and Segall (1987).

For this purpose, a single pressurized fracture of fixed height is considered in an infinite elastic medium. The fracture length is $2a = 121.92$ m and the fracture height is 1219.2 m. Because the fracture height is much greater than the fracture length, the fracture can be considered as a 2D plane strain fracture. Uniform net pressure of $\sigma_{33} = 2$ MPa is applied to the fracture faces. The uniform shear stress inside the fracture is $\sigma_{13} = 0.5$ MPa.
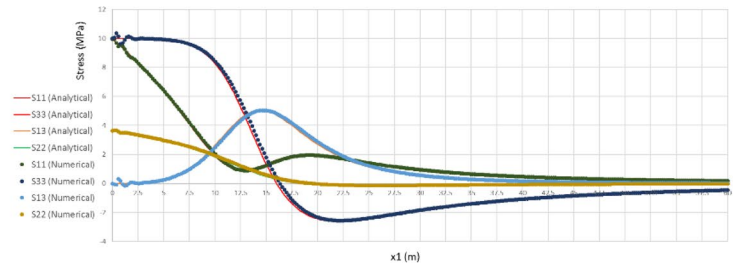
The analytical solution for the normal and shear displacement discontinuities for a plane strain fracture under uniform internal normal and shear stresses is (Pollard and Segall 1987)

$$D_n = \frac{2(1-\nu)}{G}\sqrt{a^2 - x_1^2}\,\sigma_{33};$$
$$D_s = \frac{2(1-\nu)}{G}\sqrt{a^2 - x_1^2}\,\sigma_{13},$$

(23)

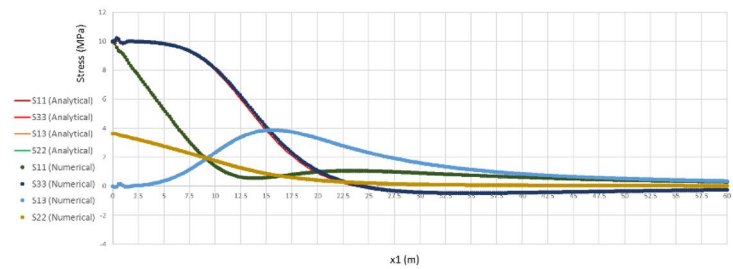**Fig. 12** Comparison of results for a fracture under plane strain conditions: stress distribution along **a** $\theta = 0°$, **b** $\theta = 30°$, **c** $\theta = 45°$, **d** $\theta = 60°$, and **e** $\theta = 90°$ (Kresse et al. 2017)
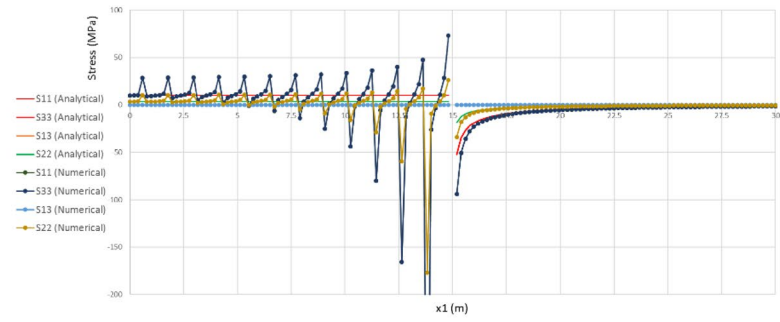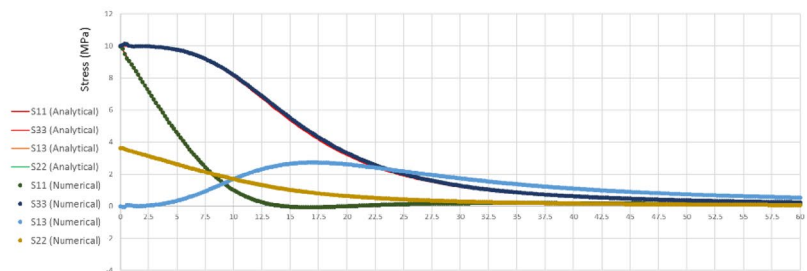
(a)
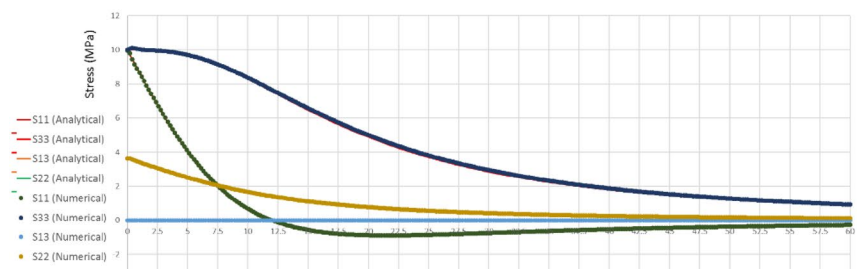
(b)

(c)

(d)

(e)

where a is the fracture half length, and σ_{33} and σ_{13} are the normal and shear stresses applied on the crack faces, correspondingly. The comparison between 3D DDM results and analytical solution is shown in Fig. 10 for the material properties $v = 0.25$, $E = 27.6$ GPa, $G = 11.04$ GPa (Kresse et al 2017).

To further validate the 3D stress shadow implementation, the analytical solution is used to calculate the normal and shear displacement discontinuities (D_n and D_s) for the given crack of length $2a = 121.92$ m subjected to constant normal and shear stresses ($\sigma_{33} = 2$ MPa and $\sigma_{13} = 0.5$ MPa). Using the computed normal and shear displacement discontinuities as known variables, the system of equations is solved for unknown normal and shear stresses. Figure 11 shows a comparison between numerical results obtained from 3D DDM and the analytical solution for the normal and shear stress distribution along the fracture length (Kresse et al. 2017). Again, the results are in good agreement with each other. It is noted that a 31×31 square element mesh (31 elements in length and 31 elements in height) was used in the simulations.
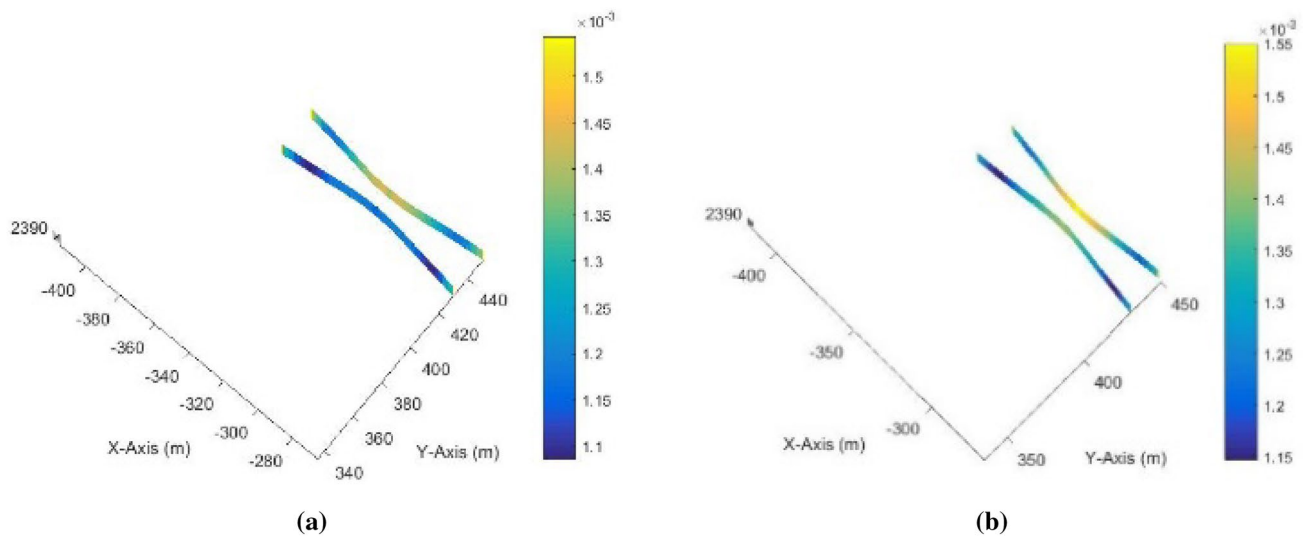

(a)   **(b)**

Fig. 13 Comparison of results for the anisotropic case with d$x=0$, d$y=10$ m: **a** 3D stress shadow and **b** 2D stress shadow

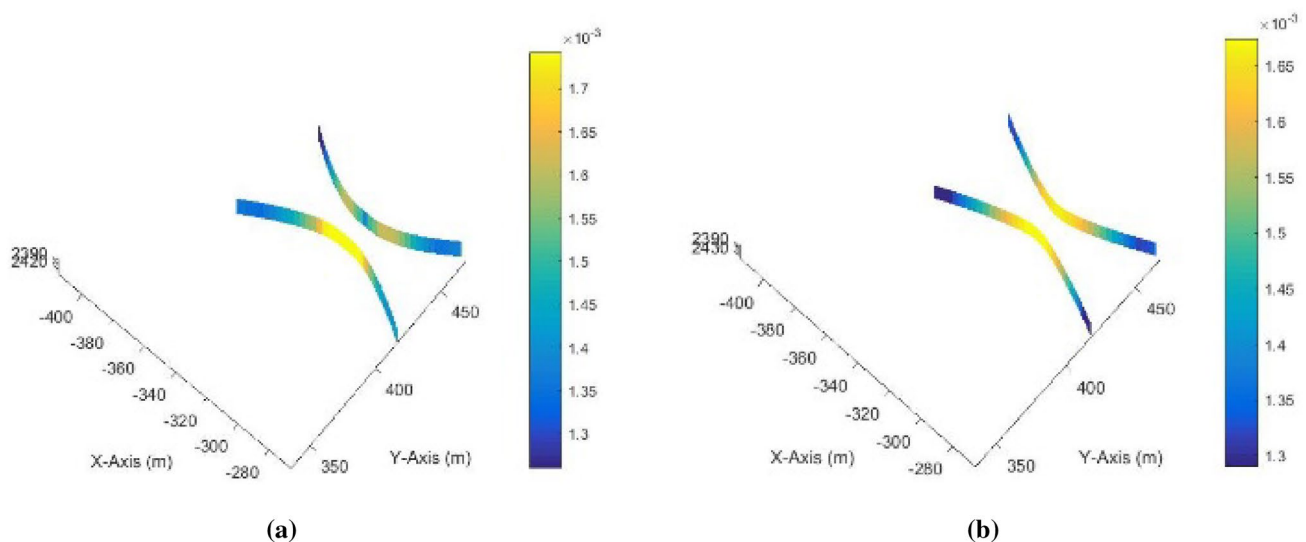**(a)**   **(b)**

Fig. 14 Comparison of results for the anisotropic case with d$x=0$, d$y=20$ m: **a** 3D stress shadow and **b** 2D stress shadow

5.2 Pressurized Fracture Under Plane Strain Conditions

In this example, the stress field around a plane strain pressurized crack of length $2a$ in a two-dimensional homogeneous, elastic medium is used to validate the 3D DDM implementation. The stress function can be used to obtain the stress field in an infinite two-dimensional elastic medium caused by the opening of an internal crack $|x| < a$ under uniform pressure p. The stress field at any point in the medium is given by (Sneddon 1946)

$$\frac{1}{2}(\sigma_x + \sigma_y) = p\left[\frac{r}{\sqrt{r_1 r_2}} \cos\left(\theta - \frac{1}{2}(\theta_1 + \theta_2)\right) - 1\right]$$

$$\frac{1}{2}(\sigma_y - \sigma_x) = p\frac{r\sin\theta}{a}\left(\frac{a}{\sqrt{r_1 r_2}}\right)^3 \sin\frac{3}{2}(\theta_1 + \theta_2) \quad (24)$$

$$\tau_{xy} = p\frac{r\sin\theta}{a}\left(\frac{a}{\sqrt{r_1 r_2}}\right)^3 \cos\frac{3}{2}(\theta_1 + \theta_2).$$

Table 1 Input data for validation against CSIRO model

Injection rate	0.1 m³/s
Stress anisotropy	0.9 MPa
Young's modulus	3×10^{10} Pa
Poisson's ratio	0.35
Fluid viscosity	0.001 Pa s
Fluid specific gravity	1.0
Min horizontal stress	46.7 MPa
Max horizontal stress	47.6 MPa
Fracture toughness	1 MPa-m$^{0.5}$
Fracture height	120 m

From which

$$\sigma_x = p\left[\begin{array}{c}\frac{r}{\sqrt{r_1 r_2}}\cos\left(\theta - \frac{1}{2}(\theta_1 + \theta_2)\right) \\ -\frac{r\sin\theta}{a}\left(\frac{a}{\sqrt{r_1 r_2}}\right)^3 \sin\frac{3}{2}(\theta_1 + \theta_2) - 1\end{array}\right]$$

$$\sigma_y = p\left[\begin{array}{c}\frac{r}{\sqrt{r_1 r_2}}\cos\left(\theta - \frac{1}{2}(\theta_1 + \theta_2)\right) \\ +\frac{r\sin\theta}{a}\left(\frac{a}{\sqrt{r_1 r_2}}\right)^3 \sin\frac{3}{2}(\theta_1 + \theta_2) - 1\end{array}\right] \quad (25)$$

$$\tau_{xy} = p\frac{r\sin\theta}{a}\left(\frac{a}{\sqrt{r_1 r_2}}\right)^3 \cos\frac{3}{2}(\theta_1 + \theta_2)$$
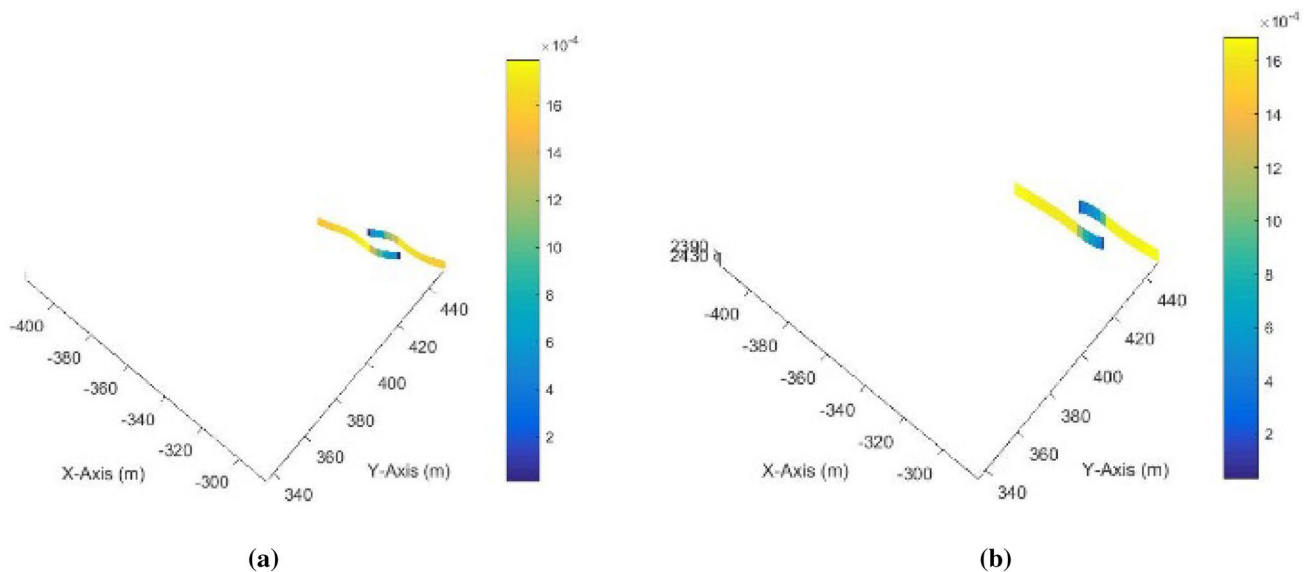
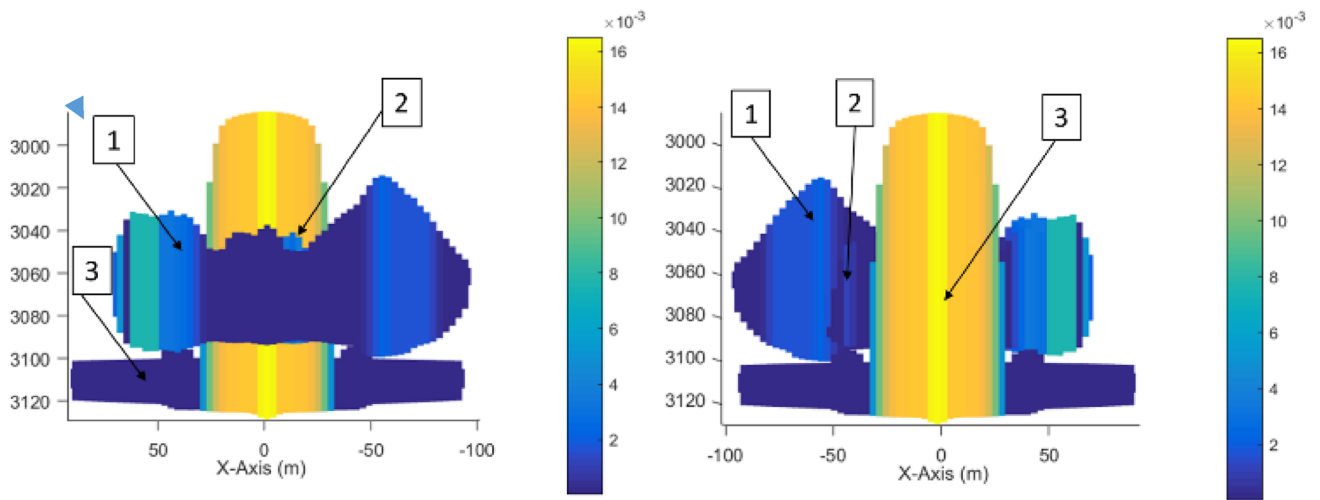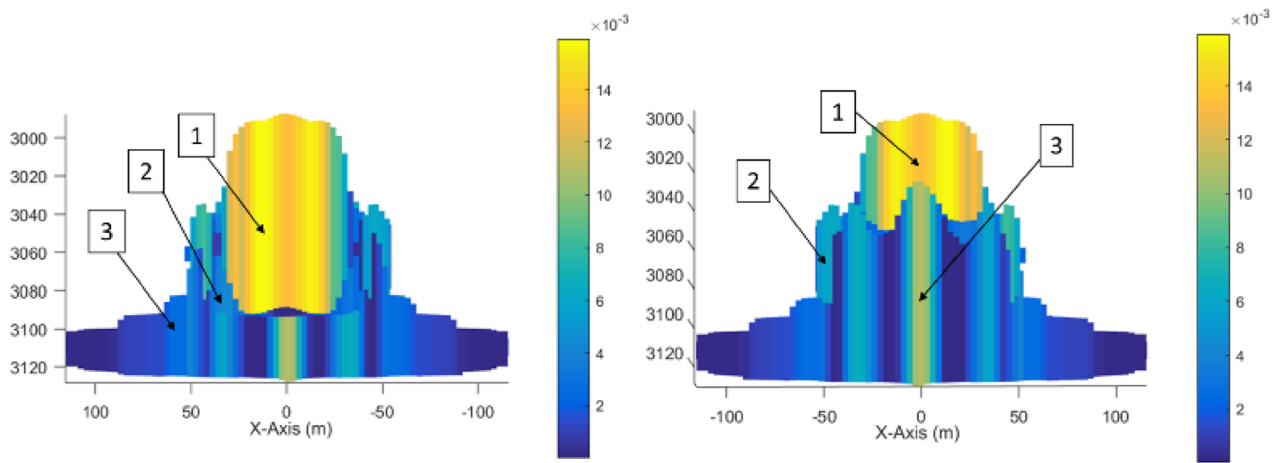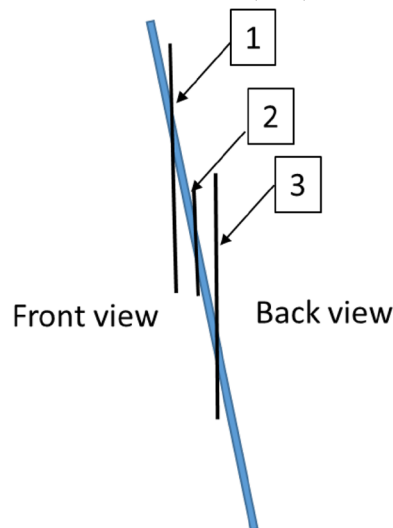$$\sigma_z = \nu(\sigma_x + \sigma_y),$$

Fig. 15 Comparison of results for the anisotropic case with dx = 10 m, dy = 20 m: **a** 3D stress shadow and **b** 2D stress shadow

**(a)** 2D Stress shadow: front (left) and back (right)

**(b)** 3D Stress Shadow: front (left) and back (right)

(c) Schematics of the fractures shown above

Fig. 16 The front (left) and back (right) view of fractures from three perforation clusters simulated with 2D (**a**) and 3D (**b**) stress shadow. The color scale represents the width of the fractures. Fractures are marked correspondingly to the perforated clusters they are initiated from **c**. **a** 2D Stress shadow: front (left) and back (right). **b** 3D Stress Shadow: front (left) and back (right). **c** Schematics of the fractures shown above
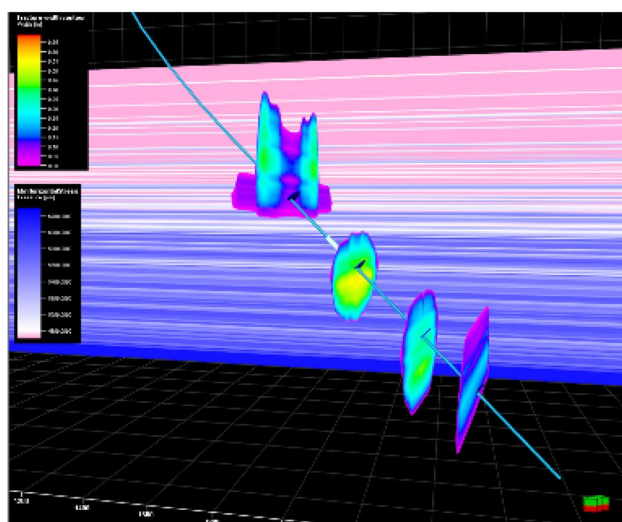
(a) 2D stress shadow
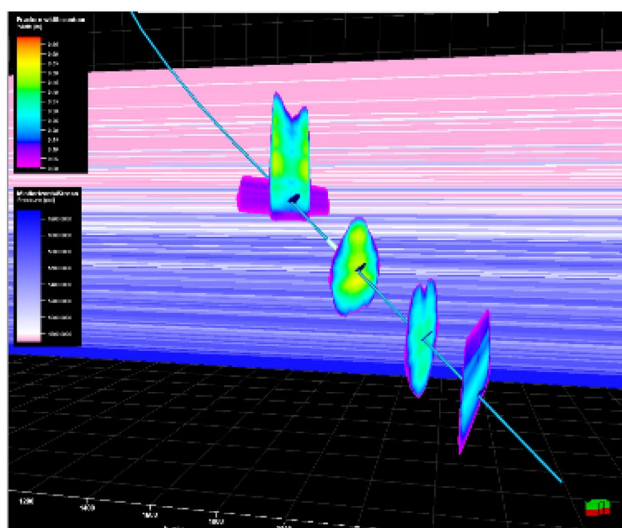
(b) 3D stress shadow

Fig. 17 Deviated well: **a** with 2D stress shadow and **b** with 3D stress shadow

where

$$x + iy = r \cos \theta + i\, r \sin \theta$$
$$(x - a) + iy = r_1 \cos \theta_1 + i\, r_1 \sin \theta_1 \qquad (26)$$
$$(x + a) + iy = r_2 \cos \theta_2 + i\, r_2 \sin \theta_2.$$

The fracture length is $2a = 30$ m, and the pressure inside the fracture is $p = 10$ MPa. Other properties of the medium are $v = 0.18$, $E = 27.6$ GPa, $G = 11.7$ GPa.

Figure 12a–e shows the stress distribution along different angles from the fracture length direction. As can be seen, the numerical results obtained from 3D DDM are in good agreement with the analytical solution with the exception

of the case of $\theta = 0°$. For the case of $\theta = 0°$, the oscillations occurred at the element boundaries due to the stress singularity associated with the constant DD kernel function.

5.3 Comparison with Numerical Solutions

The 2D cases used below for comparison have already been validated against the numerical results from a 2D DDM-based hydraulic fracture simulator incorporating a full solution of the coupled elasticity and fluid flow equations by CSIRO (Zhang et al. 2007; Kresse et al. 2012). In this section, the 3D stress shadow results are compared with the 2D stress shadow results (Figs. 13, 14, 15, Kresse et al. 2017; Table 1).

2D and 3D results are in good agreement with each other for the considered cases.

### 5.4 Effect of 3D Stress Shadow on Vertical Fracture Propagation

As it was discussed above, the 3D stress shadow allows better prediction of the fracture width profile and height. The 3D stress shadow effect is calculated at the center of each zone at the receiver's location, and gives a piece-wise constant vertical stress profile update (Fig. 4b). The contribution is compressive at the depth of the source element, and tensile above and below it.

3D stress shadow will allow us to simulate the interaction between vertically offsetting fractures in vertical or deviated wells more accurately. The examples presented below include the cases for fractures propagating mostly in viscosity dominant regimes.

5.5 Three Clusters in Vertical Well

The comparison of the results for runs with 2D stress shadow and 3D stress shadow options for the three-cluster case is shown on Fig. 16 (Kresse et al. 2017).

Three clusters are initiated from the almost vertical well with a small horizontal offset of 1.79 m. The first (1) cluster is initiated at depth of 3060 m, second (2) cluster at 3086 m, and third (3) cluster at 3109 m. Results from 3D stress shadow simulations are shown at the bottom (Fig. 16b), while 2D stress shadow simulations are on the top (Fig. 16a). The front (left) and back (right) views are presented to better understand the results. As we can see, the fracture 3 cannot grow in height in 3D stress shadow case because of the effect of the stress shadow from fractures 1 and 2. Fracture 1 in turn, also cannot grow down due to the 3D stress shadow from fracture 3, so it is pushed to grow up, while fracture 3 is pushed to grow down. These effects could not be properly captured by the 2D stress shadow.
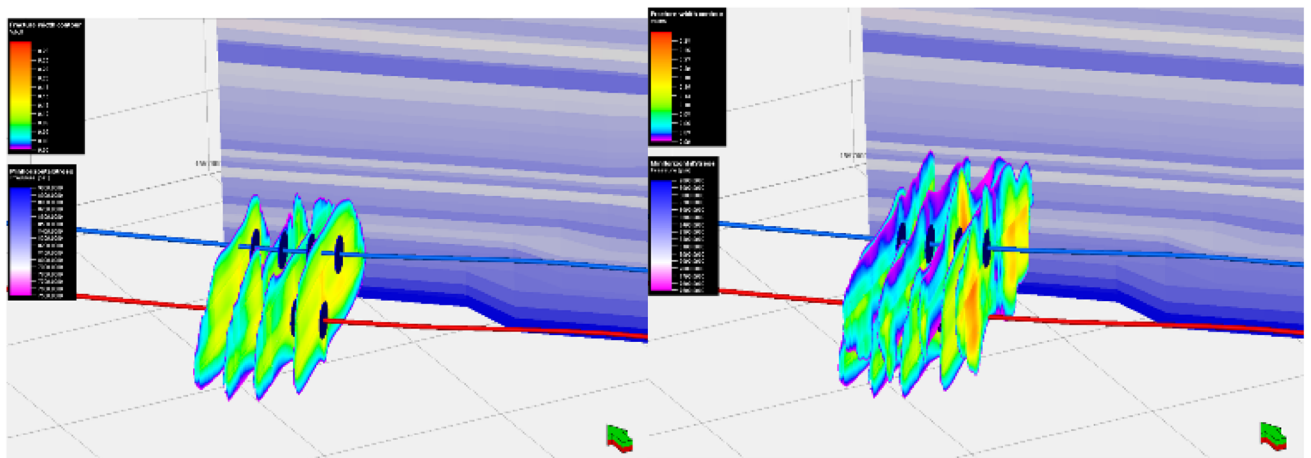
(a) 2D stress shadow: only stage 1 lower well (left), and also stage (2) at upper well (right)
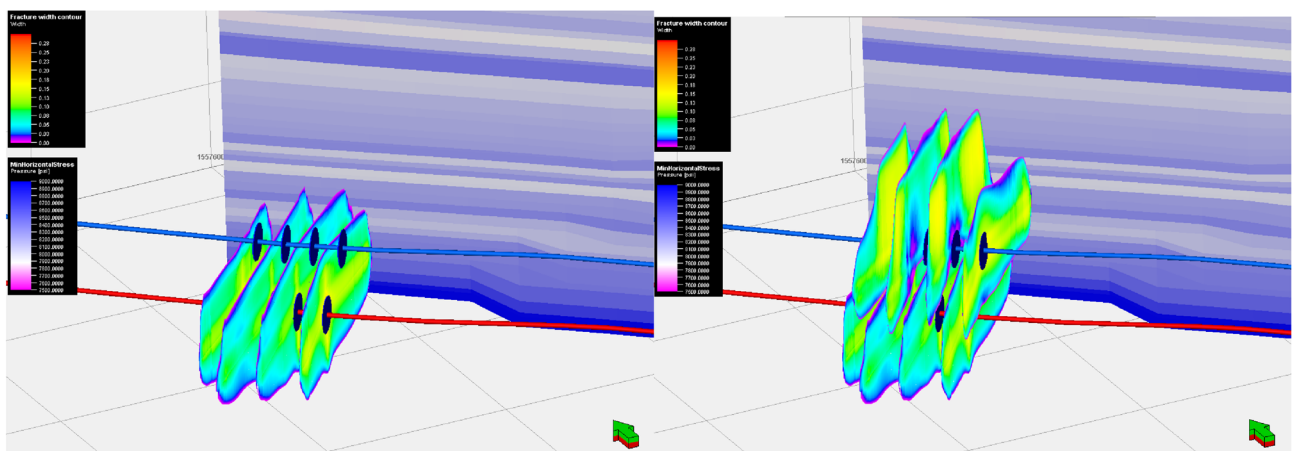
(b) 3D stress shadow: only stage 1 lower well (left), and also stage (2) at upper well (right)

Fig. 18 Stacked horizontal wells with: **a** 2D stress shadow and **b** 3D stress shadow. Stage 1 (lower well) is shown at the left, and both stages 1 and 2 are shown at the right

5.6 Multistage Case in Deviated Well

A multistage case (one cluster per stage) with four stages fractured sequentially from bottom to top is shown in Fig. 17.

The stress shadow effect from previous stages is taken into account, and results from 3D stress shadow and 2D stress shadow simulations are shown for comparison. Note that the in situ stress variation is shown in the background. Due to stress shadow effect of the still open fracture in stage 1, the fracture in stage 2 shows more upward growth for the 3D stress shadow case (Fig. 17b) than the 2D stress shadow (Fig. 17a). Similarly, more pronounced upward growth is also seen in the fracture 3 for the 3D stress shadow case. Fracture 4 has narrower width around perforation for the 2D stress shadow case due to the inaccurate vertical distribution of the induced stress explained in Fig. 2. In contrast,

3D stress shadow shows more realistic fractures shape and width profile.

5.7 Stacked Horizontal Well

The 3D stress shadow approach will also allow to better simulate the interference between fracturing stages in stacked horizontal wells targeting different layers in close proximity.

Figures 18 and 19 show an example in which the 4-cluster stage in the lower well is first fractured, followed by fracturing of the 4-cluster stage in the upper well, using 2D (Fig. 18a) and 3D (Fig. 18b) stress shadow computation, respectively, to account for the fracture interaction between clusters and between stages.

Even with the induced stress by the fractures from the lower well, the stage 1 fractures from the upper well still have significant downward growth predicted by the 2D
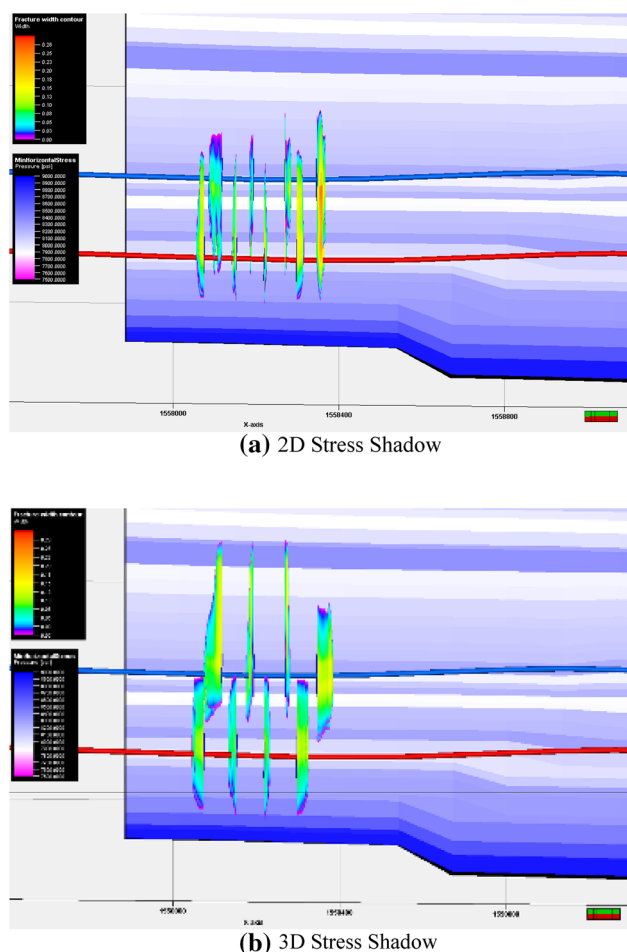
(a) 2D Stress Shadow

(b) 3D Stress Shadow

Fig. 19 Stacked horizontal wells – side view orthogonal to the wells: **a** 2D stress shadow results, **b** 3D stress shadow results for both stages

stress shadow approach due to the slightly lower stress in the lower zones (Fig. 19a). The significant width and height oscillations due to the strong interaction between fractures are also observed (Fig. 18a, left). With the 3D stress shadow, the fractures from the upper well have more upward growth due to the more accurate account of the stress shadow from the lower fractures, compared to 2D stress shadow case (Fig. 19b). This reflects more accurate and realistic vertical variation of the induced stress.

6 Conclusions

In the 3D stress shadow calculations which are based on the 3D displacement discontinuity method (DDM), each vertical element is divided into a fixed number of DD elements, with normal DD from the width profile and shear DD computed by solving from zero shear stress condition on the fracture face. Stress shadow at the center of each zone at each element's location is calculated and added to the in situ stress

profile. Stress ahead of the fracture tips is also calculated from shear and normal DDs.

Both 2D and 3D stress shadow options are implemented in a P3D-based complex fracture network model. Results show that the width profile and height growth are calculated more accurately with 3D DDM approach especially for the situations of significantly vertically offsetting perforations/ stages such as for deviated/vertical wells, and stacked horizontal wells.

References

Adachi J, Siebrits E, Peirce A, Desroches J (2007) Computer simulation of hydraulic fractures. Int J Rock Mech Min Sci 44:739–757

Carter E (1957) Optimum fluid characteristics for fracture extension. In: Howard G, Fact C (eds) Drilling and production practices. American Petroleum Institute, Tulsa, pp 261–270

Cohen CE, Kresse O, Weng X (2015) A new stacked height growth model for hydraulic fracturing simulation. ARMA 15–73, presented at 49th US Rock Mechanics Symposium, San Francisco, CA, 28 June–1 July

Crouch SL, Starfield AM (1983) Boundary element methods in solid mechanics, 1st edn. George Allen & Unwin Ltd, London

Detournay E, Cheng AH-D (1993) Fundamentals of poroelasticity. In: Fairhurst C (ed) Chapter 5 in comprehensive rock engineering: principles, practice and projects, vol II, analysis and design method. Pergamon Press, Oxford, pp 113–171

Fung RL, Vilayakumar S, Cormack DE (1987) Calculation of vertical fracture containment in layered formations. SPE Formation Eval 2(4):518–522. https://doi.org/10.2118/14707-PA

Kresse O, Weng X, Wu R, Gu H (2012) Numerical modeling of hydraulic fracture interaction in complex naturally fractured formations. ARMA12-292. https://doi.org/10.1007/s00603-012-0359-2

Kresse O, Weng X, Chuprakov D, Prioul R, Cohen CE (2013) Effect of flow rate and viscosity on complex fracture development in UFM model. International conference for effective and sustainable hydraulic fracturing, Brisbane, Australia, 20–22 May

Kresse O, Weng X, Mohammadnejad T (2017) Modeling the effect of fracture interference on fracture height growth by coupling 3D Displacement Discontibuity Methid in hydraulic fracture simulator. ARMA17-741, presented at 51st US Rock mechanics/Geomechanics Symposium, San Francisco, CA, 25–28 June

Laubach SE, Olson JE, Gale JFW (2004) Are open fractures necessarily aligned with maximum horizontal stress?. Earth Planet Sci Lett 222 (1):191–195

Mack MG, Warpinski NR (2000) Mechanics of hydraulic fracturing. In: Economides MJ, Nolte KG (eds) Chapter 6, reservoir stimulation, 3rd edn. Wiley, New York

Nolte KG, Economides MJ (eds) (2000) Reservoir stimulation. Wiley, Chichester

Olson JE (2004) Predicting fracture swarms—the influence of subcritical crack growth and the crack-tip process zone on joints spacing in rock. In: Cosgrove JW, Engelder T (eds) The initiation, propagation and arrest of joints and other fractures, vol 231. Geological Soc. Special Publications, London, pp 73–88. https://doi.org/10.1144/gsl.sp.2004.231.01.05

Olson JE (2008) Multi-Fracture propagation modeling: applications to hydraulic fracturing in shales and tight sands. 42nd US Rock

Mechanics Symposium and 2nd US-Canada Rock Mechanics Symposium, San Francisco, CA, June 29–July 2

Pollard DD, Segall P (1987) Theoretical displacements and stresses near the fractures in rock: with applications to faults, joints, veins, dikes, and solution surfaces. Fracture Mech Rock. https://doi.org/10.1016/b978-0-12-066266-1.50013-2

Rongved L (1957) Dislocation over a bounded plane area in an infinite solid. J Appl Mech 24:252–254

Salamon MD (1964) Elastic analysis of displacements and stresses induced mining of seam or roof deposits. J S Afr Inst Min Metall Part 4 65:319–338

Shou KJ (1993) A higher order three-dimensional displacement discontinuity method with application to bonded half-space problems. PhD Thesis, University of Minnesota

Shou KJ, Siebrits E, Crouch SL (1997) A higher order displacement discontinuity method for three-dimensional elastostatic problems. Int J Rock Mech Min Sci 34:317–322. https://doi.org/10.1016/s0148-9062(96)00052-6

Sneddon IN (1946) The distribution of stress in the neighborhood of a crack in an elastic solid. Proc Royal Soc A187:229–260. https://doi.org/10.1098/rspa.1946.0077

Wu K (2014) Numerical modeling of complex hydraulic fracture development in unconventional reservoirs. *PhD Thesis*, University of Texas at Austin, Texas

Wu K, Olson JE (2015) A simplified three-dimensional displacement discontinuity method for multiple fracture simulations. Int J Fract. https://doi.org/10.1007/s10704-015-0023-4

Zhang X, Jeffrey RG, Thiercelin M (2007) Deflection and propagation of fluid-driven fractures at frictional bedding interfaces: a numerical investigation. J Struct Geol 29:396–410